The Rho effector ARHGAP18 coordinates a Hippo pathway feedback loop through YAP and Merlin to regulate the cytoskeleton and epithelial cell polarity.

Emma C. Murray*[,1], Gillian M. Hodge*[,1], Khanh Pham[2], Leighton S. Lee[1], Cameron A.R. Mitchell[3], Yongho Bae[2], Andrew T. Lombardo[1,#]

*These authors contributed equally

[#] Corresponding author:

Email: Atlombar@buffalo.edu

[1] Department of Biochemistry, State University of New York at Buffalo, Buffalo N.Y.

[2] Department of Pathology and Anatomical Sciences, State University of New York at Buffalo, Buffalo N.Y.

[3] Department of Molecular Biology and Genetics, Cornell University, Ithaca N.Y.

Abstract:

The organization of the cell's cytoskeletal filaments is coordinated through a complex network of signaling cascades activated by both internal and external cues. Two major actin regulatory pathways are signal transduction through Rho family GTPases and growth and proliferation signaling through the Hippo pathway. These two pathways define the actin cytoskeleton, controlling foundational cellular attributes such as morphology and polarity and are hijacked to promote proliferation and motility in aggressive cancers. In this study, we use human epithelial cells to investigate the interplay between the Hippo and Rho Family signaling pathways, which have predominantly been characterized as independent actin regulatory mechanisms. We identify that the RhoA effector, ARHGAP18, forms a complex with the Hippo pathway transcription factor YAP to address a long-standing enigma in the field. Using super resolution STORM microscopy, we characterize single-filament-level changes in the actin cytoskeleton that arise from CRISPR/CAS9 knockout of ARHGAP18. We report that the loss of ARHGAP18 results in cytoskeletal alterations driven by both dysregulated RhoA signaling and aberrant nuclear localization of YAP. These findings indicate that the Hippo and Rho family GTPase signaling cascades are temporally and spatially coordinated in their regulation of the actin cytoskeleton.

Introduction

Extracellular signals are transduced through the cell membrane, in part through receptor ligand activation of Rho family GTPases. Rho family proteins bind and cycle between an active, guanosine triphosphate (GTP) bound, and an inactive guanosine

44 diphosphate (GDP) bound state. This cycling has traditionally been referred to as a
45 'molecular switch' that turns on or off major actin regulatory components (Hall and Nobes,
46 2000). These components include the actin-based molecular motor non-muscle myosin
47 2 (NM-2) through Rho Associated Kinase (ROCK) or the actin severing protein cofilin,
48 through LIM kinase (Julian and Olson, 2014). Recent understanding has advanced the
49 'on/off' characterization of Rho GTPases to a more nuanced regulatory environment
50 where both GTP and GDP bound states promote molecular interactions temporally and
51 spatially (Denk-Lobnig and Martin, 2019). None-the-less, Rho family GTPases are well
52 established as essential cellular signals for actin nucleation, polymerization, and
53 organization into higher-order branched or bundled structures (Hall, 1998). These signals
54 serve to order the cell into polarized domains, defining the shape of the cell, the
55 morphological structures present (e.g. microvilli, filopodia, etc.), and the cell-cell contacts
56 required to build tissues.

57 Recently, a conserved mechanism of actin regulation has emerged where domain-
58 specific regulation by Rho effectors is controlled on a minute temporal and spatial scale
59 (Jackson et al., 2024; Landino et al., 2021; Sepaniac et al., 2023; Swider et al., 2022).
60 Our group recently characterized an epithelial specific RhoA signaling pathway involving
61 ARHGHAP18 organizing at the apical surface of polarized cells on the scale of 100nm
62 (Lombardo et al., 2024). Separately, we showed in human colorectal CaCo-2 cells that
63 the RAB GAP Epi64A localizes to an approximately 75nm region at the base of microvilli
64 to regulate the terminal web of actin controlling cell shape (Miller et al., 2022). Collectively,
65 these findings indicate that from flies to humans, the cell regulates Rho family GTPases
66 on the scale of each individual actin structure to build the correct structure at the correct

67 time. In the progress of our studies, we discovered an unexpected phenotype in cells
68 genetically lacking ARHGAP18. These cells exhibited a basal membrane actin phenotype
69 opposite to what would be expected from the loss of a RhoA GAP, challenging the
70 emerging model in the field.

71 ARHGAP18 shows a strong specificity for accelerating the hydrolysis of GTP of
72 RhoA in epithelial cells (Maeda et al., 2011) but also exhibits increased activity toward
73 RhoC in endothelial cells (Chang et al., 2014). RhoA-GTP regulates the actin
74 cytoskeleton by promoting multiple downstream kinase pathways. Of these, two kinases
75 are required for the formation actin organization in polarized epithelial cells: Rho-
76 associated protein kinase (ROCK) and the homologues Lymphocyte Oriented Kinase/
77 STE20-like Kinase (LOK/SLK). These kinases increase actin bundling in both stress
78 fibers through non-muscle myosin-2 (NM-2) and microvilli through activation of the Ezrin,
79 Radixin, Moesin (ERM) family in concert with recruitment of additional microvilli specific
80 components (Gaeta et al., 2021; Morales et al., 2023; Zaman et al., 2021). RhoA GAPs
81 limit these effects by accelerating the transition of RhoA, negatively regulating them
82 toward its inactivated GDP-bound state. Thus, increased RhoA GAP activity canonically
83 scales inversely with the formation of bundled actin filaments. However, ARHGAP18
84 knockdown results in the disorganization of stress fibers in human cells (Lay et al., 2019).
85 The fly homolog of ARHGAP18 was similarly reported to positively regulate actin bundling
86 through Rho1 and was subsequently named conundrum (Conu) due to this unexpected
87 phenotype (Neisch et al., 2013). Astonishingly, knockdown of ARHGAP18 in human 3D
88 spheroids was reported to reduce NM-2 activation and resulted in a loss of stress fibers
89 (Porazinski et al., 2015).

90 To explain these results, ARHGAP18 is hypothesized to act as a non-traditional
91 RhoA GAP where genetic screening linked its enigmatic function to the cytoskeletal
92 transcription factor Yes-associated protein (YAP) (Porazinski et al., 2015). Additionally, in
93 ARHGAP18 deleted mice, YAP inappropriately localizes to the nucleus (Coleman et al.,
94 2020). YAP and the transcriptional co-activator with PDZ-binding motif (TAZ) are the
95 downstream effectors of the Hippo pathway. Hippo signaling originates with
96 mechanosensation and nutrient availability at apical and junctional membranes in part
97 through the ERM-related protein Merlin (also known as neurofibromin 2 or NF2) (Harvey
98 et al., 2013; Reginensi et al., 2016). Hippo signaling shuttles YAP and TAZ between the
99 cytoplasm and nucleus. When localized to the nucleus, YAP/TAZ promotes the activation
100 of cytoskeletal transcription factors associated with cell proliferation and actin
101 polymerization. Phosphorylation of YAP at the S127 residue targets it to the cytoplasm
102 for eventual degradation. Alternatively, the activation of YAP and TAZ is pervasive in
103 human malignancies (Zanconato et al., 2016). The combined results of the studies linking
104 ARHGAP18 to YAP/TAZ reported both upstream and downstream regulation, indicating
105 a possible feedback loop. However, the mechanism of this potential relationship remained
106 unknown.

107 In this manuscript, we characterize the aberrant actin networks of Jeg-3 human
108 epithelial cells genetically lacking ARHGAP18. Using super resolution STORM to resolve
109 the actin filament network to a resolution of <40nm, we report that loss of ARHGAP18
110 results in a near total loss of basal actin bundles, including stress fibers and filopodia. We
111 characterize the alterations to the kinases downstream of RhoA signaling regulating basal
112 actin organization. Our results indicate that the defective basal actin organization results

113 from both RhoA regulation through canonical GAP activity and separately through
114 ARHGAP18's regulation of YAP localization. We report that ARHGAP18 forms a stable
115 complex with YAP, which regulates its cytoplasmic to nuclear shuttling to control basal
116 actin organization. Further, ARHGAP18 binds to Merlin, enabling ARHGAP18 to act as a
117 feedback system for the Hippo signaling pathway. This mechanism allows the cell to
118 coordinate the Hippo and Rho family signaling pathways to regulate the actin cytoskeletal
119 organization in response to both internal and external cues.

120 **Results:**

121 **ARHGAP18 Regulates Non-Muscle Myosin-2 Through a RhoA Independent**
122 **Mechanism**

123 Our group recently characterized the regulation of microvilli through direct binding
124 of ARHGAP18 to Ezrin, where we produced and validated CRISPR/CAS9 knock out of
125 ARHGAP18 in human epithelial Jeg-3 cells (Fig. 1A) (Lombardo et al., 2024). In microvilli,
126 ARHGAP18 acts to suppress active RhoA leading to reduced ROCK activation and lower
127 MLC phosphorylation. Surprisingly, cells lacking ARHGAP18 and cells overexpressing
128 ARHGAP18 both show increased phosphorylation of myosin light chain (Fig. 1B). Total
129 expression levels of NM-2, total MLC, and actin are unchanged across these conditions
130 (Fig. 1B). We hypothesized that the overexpression of ARHGAP18 was regulating the
131 downstream RhoA kinase ROCK independent of its GAP activity. To probe this possibility,
132 we tested if the alternative signaling cascades downstream of ROCK were functioning
133 properly. Using phosphospecific antibodies for western blotting, we detected that
134 phosphorylation of LIM kinase (pLIMK) and cofilin (pCofilin) exhibited only minor changes
135 in the absence of ARHGAP18 (Fig. 1C, D). While the abundance of phosphorylated LIMK

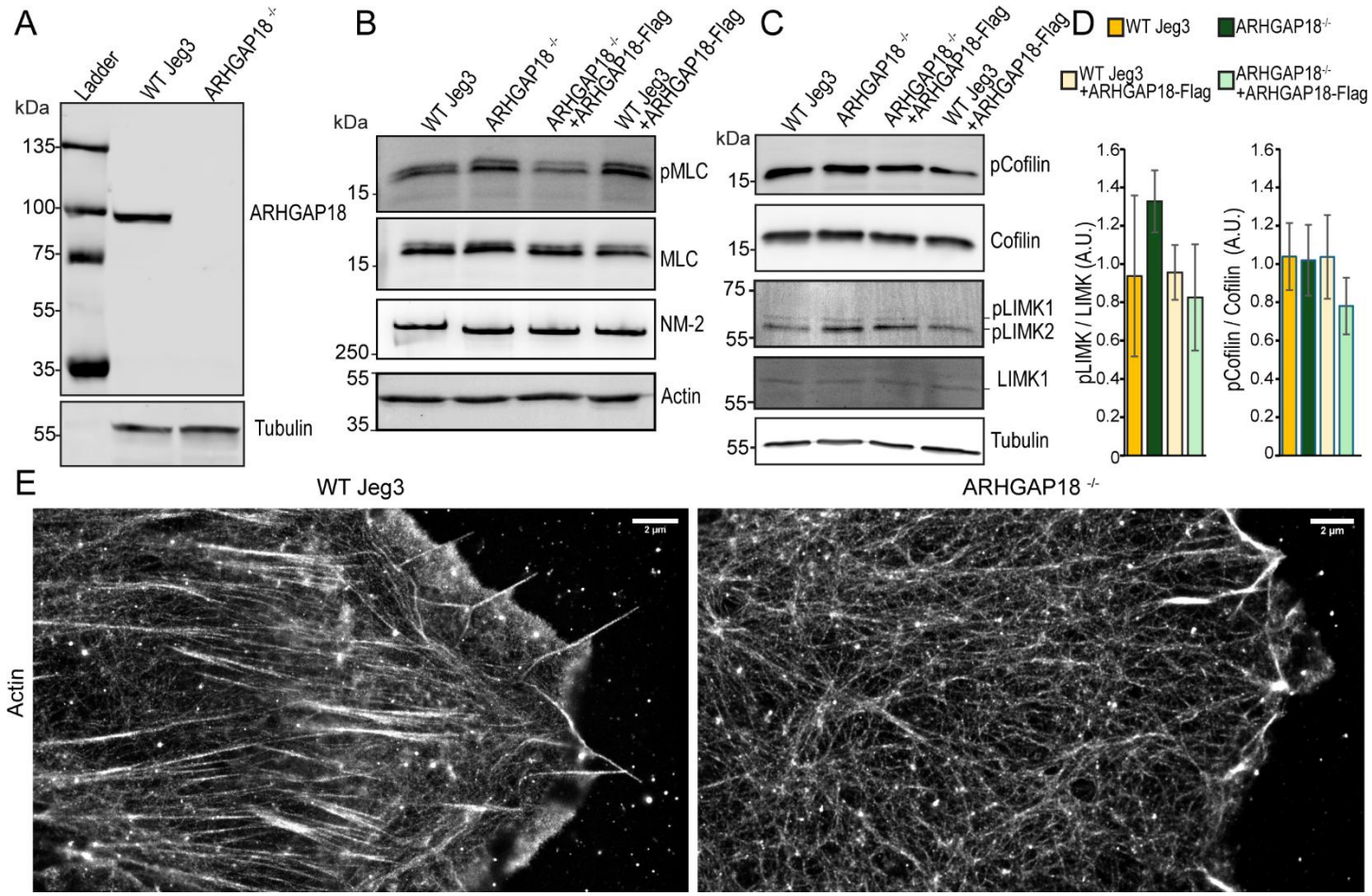

Figure 1: Characterization of ARHGAP18 Knockout in Human Epithelial Cells. A) Western blot of ARHGAP18 and Tubulin in WT Jeg-3 cells and ARHGAP18$^{-/-}$ knockout (KO) cells. B) Western blot of Non-muscle Myosin 2 (NM-2), Myosin Light Chain (MLC), and phosphorylated MLC (pMLC) in WT and KO cells with tagged ARHGAP18 rescue or overexpression. C) Western blot of total cofilin and LIM kinase vs. phosphorylated fractions of each in the same conditions as (B). D) Quantification of western blot intensity of the ratio of phosphorylated fraction over total for cofilin and LIMK in the conditions from (C). Bars indicate Mean±SEM; All conditions non-significant by t-test ($p>0.05$) n=3 E) STORM reconstructions of phalloidin stained Actin in fixed Jeg-3 WT and Jeg-3 ARHGAP$^{-/-}$ cells. Scale bar 2µm.

136 appeared slightly increased in the KO cells, it did not rise to the level of statistical
137 significance. Unlike pMLC, over-expression of ARHGAP18 resulted in only a modest
138 decrease in phosphorylation of LIM kinase and Cofilin (Fig. 1D), which was not
139 significantly different than WT cells. We concluded that in ARHGAP18 altered cells LIMK,
140 Cofilin, and MLC were in part regulated through the RhoA GAP activity of ARHGAP18.
141 However, MLC in the ARHGAP18 overexpression was regulated through a GAP-
142 independent mechanism.

143 **Cells Lacking ARHGAP18 have disorganized basal actin and a loss of focal**
144 **adhesions**

145 Increased pMLC in the absence of ARHGAP18 is expected to result in increased
146 stress fiber formation through the activation of NM-2. However, multiple independent
147 investigations, including our own, had identified the loss of stress fibers in cells with
148 reduced or lacking ARHGAP18 (Lay et al., 2019; Lombardo et al., 2024; Neisch et al.,
149 2013; Porazinski et al., 2015). However, the true structure of actin filaments is well below
150 the diffraction limited resolution of light, which forms dense arrays of filaments at the
151 plasma membrane cortex interface. To characterize the actin filament organization at the
152 basal surface of cells lacking ARHGAP18, we employed Stochastic Optical
153 Reconstruction Microscopy (STORM) to resolve the individual actin architecture to a
154 spatial X-Y resolution of less than 40nm. WT Jeg-3 cells showed numerous stress fiber
155 bundles at the basal surface of the cell (Fig. 1E). Actin filaments transitioned to lateral
156 filaments running parallel to the plasma membrane and eventually to a canonical leading
157 edge comprised of both cortical branched individual filaments and filopodia at the cell's
158 plasma membrane. The orientation of the stress fibers and filopodia generally aligned in

159 the axis going from cell center to cell exterior. In contrast to the WT actin organization,
160 cells lacking ARHGAP18 exhibit a striking absence of both stress fibers and filopodia (Fig.
161 1E). The actin of ARHGAP18 KO cells was organized into small bundles and long
162 individual filaments. Notably, the orientation of the ARHGAP18 KO cells' actin was
163 substantially less aligned in the general axis going from cell center to cell exterior seen in
164 the WT cells.

165 To further characterize the basal actin phenotype in cells devoid of ARHGAP18
166 further, we used immunofluorescent staining of NM-2B using spinning disk confocal.
167 Stress fibers from WT cells showed actin colocalized with repeating striations of NM-2B
168 indicative of active, contractile fibers (Fig. 2A). NM-2B still colocalized to actin in
169 ARHGAP18 deficient cells but organized into smaller more diffuse puncta. We previously
170 reported that ARHGAP18-deficient cells were nearly twice as stiff as WT cells when
171 measured by force indentation using atomic force microscopy (Lombardo et al 2024).
172 Given these data combined with our western blotting of pMLC, we concluded that NM-2B
173 was still active in cells lacking ARHGAP18 and capable of forming into contractile bundles
174 but that the force-producing activity was not organizing the actin into large stress fiber
175 bundles seen in the WT cells.

176 To investigate why basal actin organization was disrupted despite the activation of
177 NM-2 in ARHGAP18 KO cells, we investigated the presence of actin to basal-membrane
178 contact proteins. Immunofluorescent imaging of Vinculin in WT cells indicated that stress
179 fibers were tethered to the plasma membrane at the basal surface (Fig.2B). Imaging of
180 ARHGAP18 $^{-/-}$ cells showed mislocalization of vinculin with no focal adhesions observed.
181 Expression of full-length human ARHGAP18-flag in ARHGAP18 $^{-/-}$ cells rescued both actin

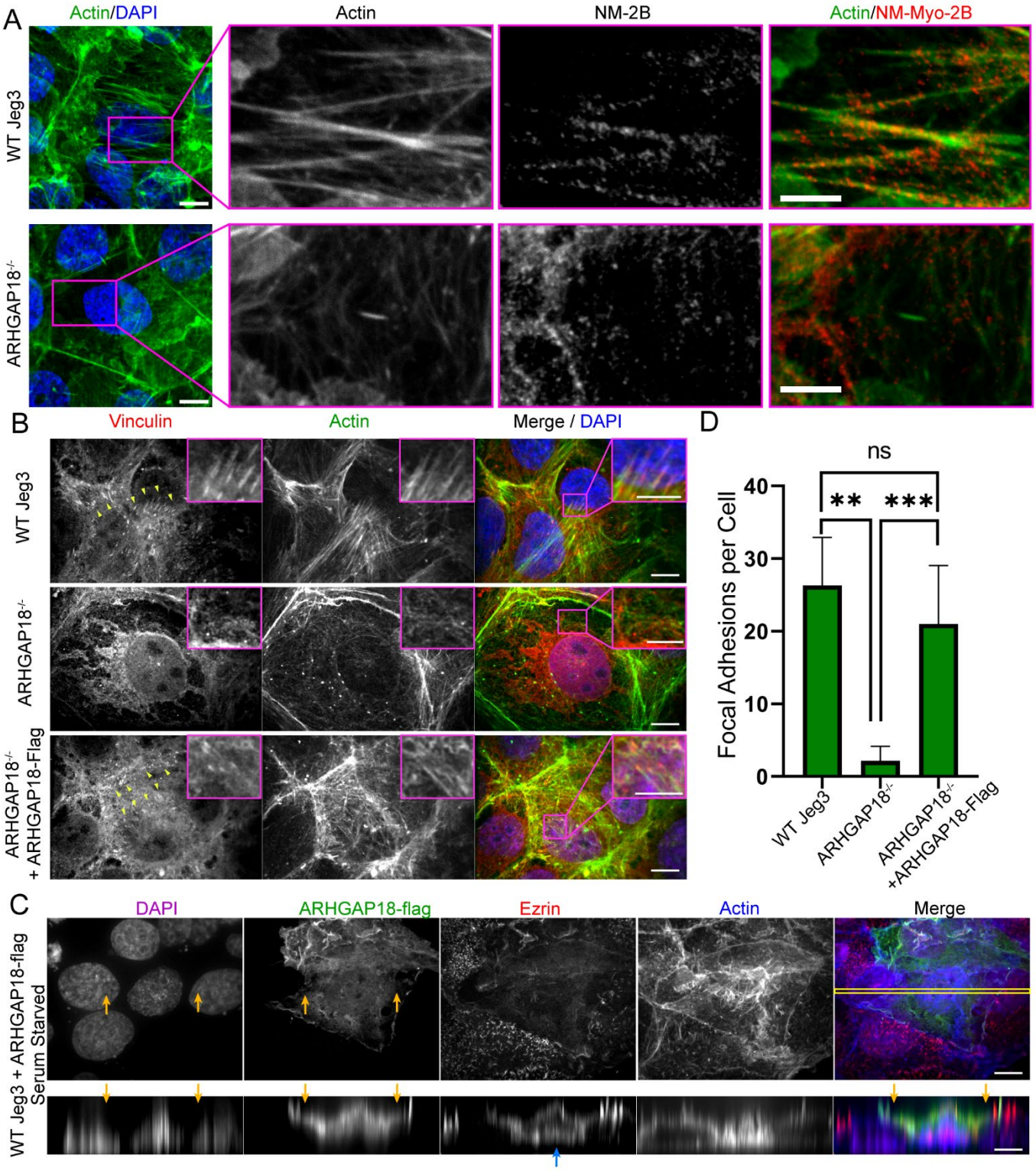
A
Actin/DAPI
Actin
NM-2B
Actin/NM-Myo-2B
WT Jeg3
ARHGAP18-/-
B
Vinculin
Actin
Merge / DAPI
WT Jeg3
ARHGAP18-/-
ARHGAP18-/- + ARHGAP18-Flag
D
ns
**
***
Focal Adhesions per Cell
40
30
20
10
0
WT Jeg3
ARHGAP18-/-
ARHGAP18-/- +ARHGAP18-Flag
C
DAPI
ARHGAP18-flag
Ezrin
Actin
Merge
WT Jeg3 + ARHGAP18-flag Serum Starved

Figure 2: ARHGAP18 Binds Merlin and Effects NM-2 and Vinculin at the Basal Surface. A) Immunofluorescent imaging of actin and Non-Muscle Myosin-2B (NM-2B) in WT and ARHGAP18$^{-/-}$ cells. Scale bar 10μm; inset 5μm B) Immunofluorescent imaging of vinculin and actin in WT and ARHGAP18$^{-/-}$ cells and ARHGAP18-flag rescue cells. Focal adhesions co-localizing actin and vinculin highlighted with yellow arrowheads. Scale bar 10μm. Inset scale bar 5μm. C) Spinning disk confocal immunofluorescent imaging of WT Jeg-3 cells overexpressing ARHGAP18-flag. Actin to plasma membrane crosslinker ezrin localizes exclusively to the apical plasma membrane. Lower image row shows the X-Z dimension of the same image showing the invasion of the overexpressing cell onto neighboring cells. Yellow arrows indicate the sections of the overexpressing cell invading over neighboring cells' nucleus. Blue arrow indicates two stacked apical membranes by ezrin staining with the lower membrane from WT cells underneath the upper membrane from an ARHGAP18 overexpressing cell. Scale bars 10μm. D) Quantification of the number of vinculin-stained focal adhesions per cell. Bars are Mean ± SEM. conditions are significant by Mann-Whitney test; WT n=average of 4 replicates, ARHGAP18$^{-/-}$ n=average of 7 replicates, ARHGAP18$^{-/-}$ +ARHGAP18-Flag n= average of 7 replicates (**= $p \leq 0.01$, *** = $p \leq 0.001$, n.s.= not significant).

182 basal actin bundles and vinculin focal adhesion localization (Fig 2B). We sought to
183 characterize the defects of pMLC overactivation and vinculin mislocalization in cells
184 overexpressing ARHGAP18-flag. However, we discovered that WT cells overexpressing
185 ARHGAP18 would often break from the surrounding Jeg-3 cell's monolayer to form three-
186 dimensional stacks of cells (Fig. 2C). This characteristic was not typically seen in
187 monolayered WT and ARHGAP18$^{-/-}$ cells (Fig. 2A). To investigate this invasive phenotype,
188 we used transient transfection of ARHGAP18-flag into WT cells which allowed us to
189 compare the behavior of WT cells side-by-side with ARHGAP18 overexpressing cells.
190 Spinning disk confocal Z-dimensional slicing of the actin on these cells indicated that large
191 basal actin bundles and stress fibers were present in the ARHGAP18 overexpression
192 cells (Fig. 2C). We observed that cells overexpressing ARHGAP18 invade their
193 neighboring cells monolayer climbing almost entirely on top of the adjacent WT cells (Fig.
194 2C yellow arrows). These data support the conclusion that ARHGAP18 acts to regulate
195 basal and junctional actin through Rho-independent mechanisms.

196 **Cells Lacking ARHGAP18 Have Transcriptional Changes in Actin and Proliferation**
197 **Regulators**

198 We hypothesized that the invasive and cytoskeletal phenotypes observed at the
199 basal surface of cells devoid of ARHGAP18 may be a result of changes in regulation at
200 the transcriptional level either directly through RhoA signaling or through an additional
201 mechanism specific to ARHGAP18. To test this hypothesis, we performed bulk RNA
202 sequencing (RNAseq) on WT-Jeg-3 and ARHGAP18 KO cells. We confirmed
203 expressional changes between WT and ARHGAP18 KO cells using PCA analysis (Fig
204 3A). The analysis revealed two distinct clusters corresponding to WT Jeg-3 and

205 ARHGAP18 KO samples, suggesting clear transcriptomic differences between the two
206 groups. A total of 889 differentially expressed genes, with 551 upregulated and 368
207 downregulated genes, were identified in ARHGAP18 KO cells compared to in WT Jeg-3
208 cells. The distribution of these DEGs was displayed in the volcano plot (Fig. 3B,
209 Supplemental Data).

210 To further explore the impact of ARHGAP18 KO on overall cell functions, we
211 performed Gene Ontology (GO) enrichment analysis and identified that across different
212 GO categories, cell morphology, migration, junctional anchoring, and actin filament
213 binding terms were significantly altered in cells lacking ARHGAP18 (Fig. 3C-E).
214 Additionally, numerous terms related to microvilli and the apical plasma membrane
215 including ion binding, lipid binding, plasma membrane binding were also enriched. To
216 investigate the expression changes of specific genes associated with these terms across
217 all of our samples, we plotted the expressional patterns of each gene into clustered
218 heatmaps (Fig. 3F-H). Microvilli specific regulators included multiple myosin motor
219 proteins responsible for membrane to plasma membrane linkages (Myo1E, Myo1D) and
220 transport of lipid and protein vesicles inside microvilli (Myo10). By comparing the proteins
221 that meet the shared characteristics of anchoring, migration and actin binding (Fig. 3I) we
222 identified LCP1, also known as L-plastin as upregulated in ARHGAP18-deficient cells.
223 Plastin-1 is a predominate actin bundler in microvilli (also called Fimbrin), while L-plastin
224 is associated with tumorigenesis when expressed outside of bone. A second gene,
225 CORO1A (Coronin 1), was also identified, which is involved with RhoA-dependent
226 signaling (Priya et al., 2016). These results are validated by our previous characterization

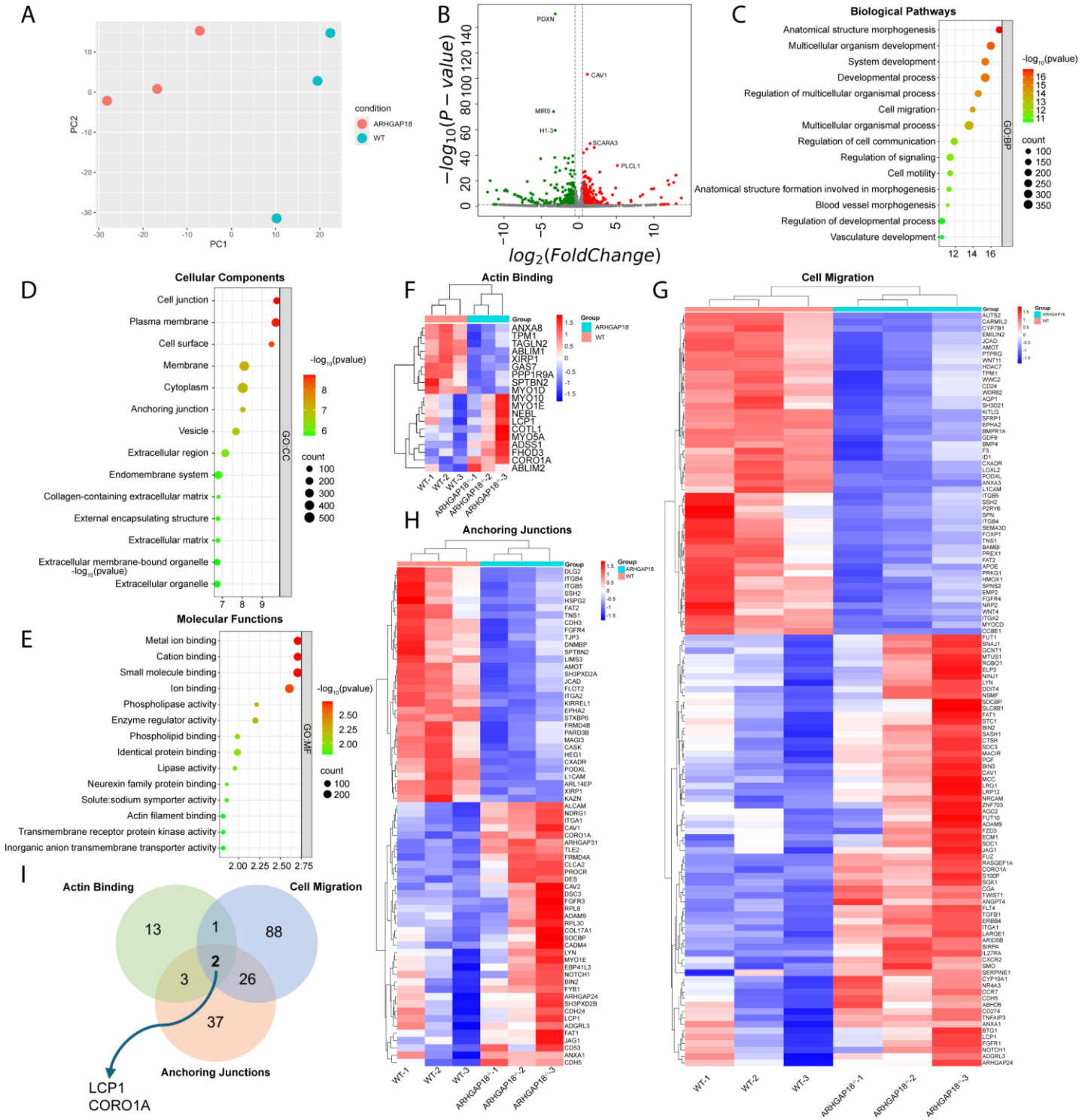
A
PC2
PC1
condition
ARHGAP18
WT
B
PDXN
CAV1
MIR9
H1-3
SCARA3
PLCL1
$-log_{10}(P-value)$
$log_2(FoldChange)$
C
Biological Pathways
Anatomical structure morphogenesis
Multicellular organism development
System development
Developmental process
Regulation of multicellular organismal process
Cell migration
Multicellular organismal process
Regulation of cell communication
Regulation of signaling
Cell motility
Anatomical structure formation involved in morphogenesis
Blood vessel morphogenesis
Regulation of developmental process
Vasculature development
GO:BP
$-log_{10}$(pvalue)
count
D
Cellular Components
Cell junction
Plasma membrane
Cell surface
Membrane
Cytoplasm
Anchoring junction
Vesicle
Extracellular region
Endomembrane system
Collagen-containing extracellular matrix
External encapsulating structure
Extracellular matrix
Extracellular membrane-bound organelle
Extracellular organelle
GO:CC
$-log_{10}$(pvalue)
count
E
Molecular Functions
Metal ion binding
Cation binding
Small molecule binding
Ion binding
Phospholipase activity
Enzyme regulator activity
Phospholipid binding
Identical protein binding
Lipase activity
Neurexin family protein binding
Solute:sodium symporter activity
Actin filament binding
Transmembrane receptor protein kinase activity
Inorganic anion transmembrane transporter activity
GO:MF
$-log_{10}$(pvalue)
count
F
Actin Binding
ANXA8
TPM1
TAGLN2
ABLIM1
XIRP1
GAS7
PPP1R9A
SPTBN2
MYO1D
MYO10
MYO1E
NEBL
LCP1
COTL1
MYO5A
ADSS1
FHOD3
CORO1A
ABLIM2
WT-1
WT-2
WT-3
ARHGAP18⁻-1
ARHGAP18⁻-2
ARHGAP18⁻-3
Group
ARHGAP18
WT
G
Cell Migration
H
Anchoring Junctions
I
Actin Binding
Cell Migration
Anchoring Junctions
13
1
88
2
3
26
37
LCP1
CORO1A

Figure 3: ARHGAP18 total RNA sequencing shows changes in transcription of actin regulatory processes including HIPPO and YAP/TAZ dependent pathways. A) Principle Component Analysis (PCA) from total RNA sequencing results obtained from WT Jeg-3 and ARHGAP18$^{-/-}$ cells (n=3) B) plot of Adjusted p-value vs. log fold change in expression (volcano plot) with select genes identified C) Go terminology analysis of biological pathways. Color indicates p-value, representing the likelihood that a pathway is altered in ARHGAP18$^{-/-}$ vs. WT Jeg-3 cells while bubble size indicates the number of genes identified with altered expression. D) GO terminology analysis of Cellular components E) GO terminology analysis of Molecular Functions. F) Heat map of the genes where the gene product is a known or predicted actin binding protein in each of the 3 biological replicates from WT Jeg-3 or ARHGAP18$^{-/-}$ cells. Color indicates fold change where blue is lower expression and red is increased expression compared to the other group. G) Heatmap similar to (F) for Cell Migration gene products H) Heatmap similar to (F) for Anchoring Junctional gene products. I) Venn diagram identifying genes that are combinations of the terms shown in (F)-(H). LCP1 and CORO1A's gene products bind actin and have been characterized to play a role at anchoring junctions and in cell migration.

227 of ARHGAP18 in the biogenesis and maintenance of microvilli at the apical membrane
228 through RhoA (Lombardo et al., 2024).

229 Further analysis of the individual gene products associated with actin, cell
230 migration, and anchoring junctions identified proteins associated with the defects we
231 previously identified in ARHGAP18 KO cells at the basal surface. Most notable among
232 these were the alterations in the expression of Integrins (ITGA1, ITGA2 INTGB5,
233 INTGB4) and other focal adhesion gene products such as TNS1(Fig. 3F-H). These results
234 are validated by our finding that ARHGAP18$^{-/-}$ cells lack focal adhesions (Fig. 2B). To
235 further investigate the relationship between genes with altered expression in ARHGAP18
236 KO, we performed network analysis using Ingenuity Pathway Analysis (IPA). Our analysis
237 revealed that some protein-protein relationships can be predicted, such as ARHGAP18's
238 regulation of RhoA (Fig. S1). However, network analysis also revealed that most
239 interactions would not be through known protein-protein interactions or through RhoA
240 signaling. These results promoted the hypothesis that the alterations defined in the
241 RNAseq data derive from alterations in transcription rather than through direct protein-
242 protein interactions. To explore this potential, we manually characterized the known
243 signaling pathways involved with all down expressed genes related to cell migration
244 (Supplemental Table 1). We found that of these genes, more than half of them were
245 associated with WNT, HIPPO, or MAPK/PI3K signaling pathways, and multiple were
246 direct YAP/TAZ effectors (Supplemental Table 1). We concluded that loss of ARHGAP18
247 was not only altering cytoskeletal organization through direct RhoA signaling but
248 additionally resulting in alterations to transcriptional signaling of and expression of
249 proteins regulating the actin cytoskeleton.

250 **ARHGAP18 regulates YAP phosphorylation and nuclear localization**

251 Multiple prior studies indicated that ARHGAP18 interacts downstream of YAP
252 through the Hippo pathway to regulate transcription of actin organization and cell
253 proliferation (Coleman et al., 2020; Porazinski et al., 2015). We hypothesized that the
254 aberrant actin organization observed in ARHGAP18$^{-/-}$ cells, along with the invasive
255 properties of overexpressing cells, resulted from a partial loss of the terminally
256 differentiated apical/basal polarity characteristic of microvilli expressing cells. One
257 possibility was the direct binding of ARHGAP18 to YAP or TAZ. A second possibility was
258 that ARHGAP18 could influence YAP through upstream Hippo pathway components. Our
259 group recently identified a short binding motif of ARHGAP18 from V10 to S17 that bound
260 directly to the FERM domain of ERMs (Lombardo et al 2024). Merlin, which localizes to
261 cell-cell junctions, acts upstream of YAP through the Hippo pathway shares a close
262 structural similarity to ERMs. We tested if ARHGAP18 could form a complex with Merlin
263 using a pull-down approach by passing lysate from WT Jeg-3 cells expressing a tagged
264 Merlin construct over an immobilized ARHGAP18 column. We found that Merlin
265 expressed in human Jeg-3 cells bound to the ARHGAP18 column (Fig. 4A). To investigate
266 this interaction, we sought to identify if ARHGAP18 was localized to junctions where
267 Merlin is active. We used the rescue of ARHGAP18 $^{-/-}$ cells with a flag tagged ARHGAP18
268 to image the localization of ARHGAP18 in serum-starved versus cells supplemented with
269 FBS for 1 hour following serum starvation (Fig. 4B). Maximum projection images of
270 ARHGAP18-flag showed localization of ARHGAP18 to microvilli at the apical surface,
271 along with the rescue of increased microvilli formation in ARHGAP18$^{-/-}$ cells as we've
272 previously reported (Fig. 4A) (Lombardo et al., 2024). Additionally, ARHGAP18 localized

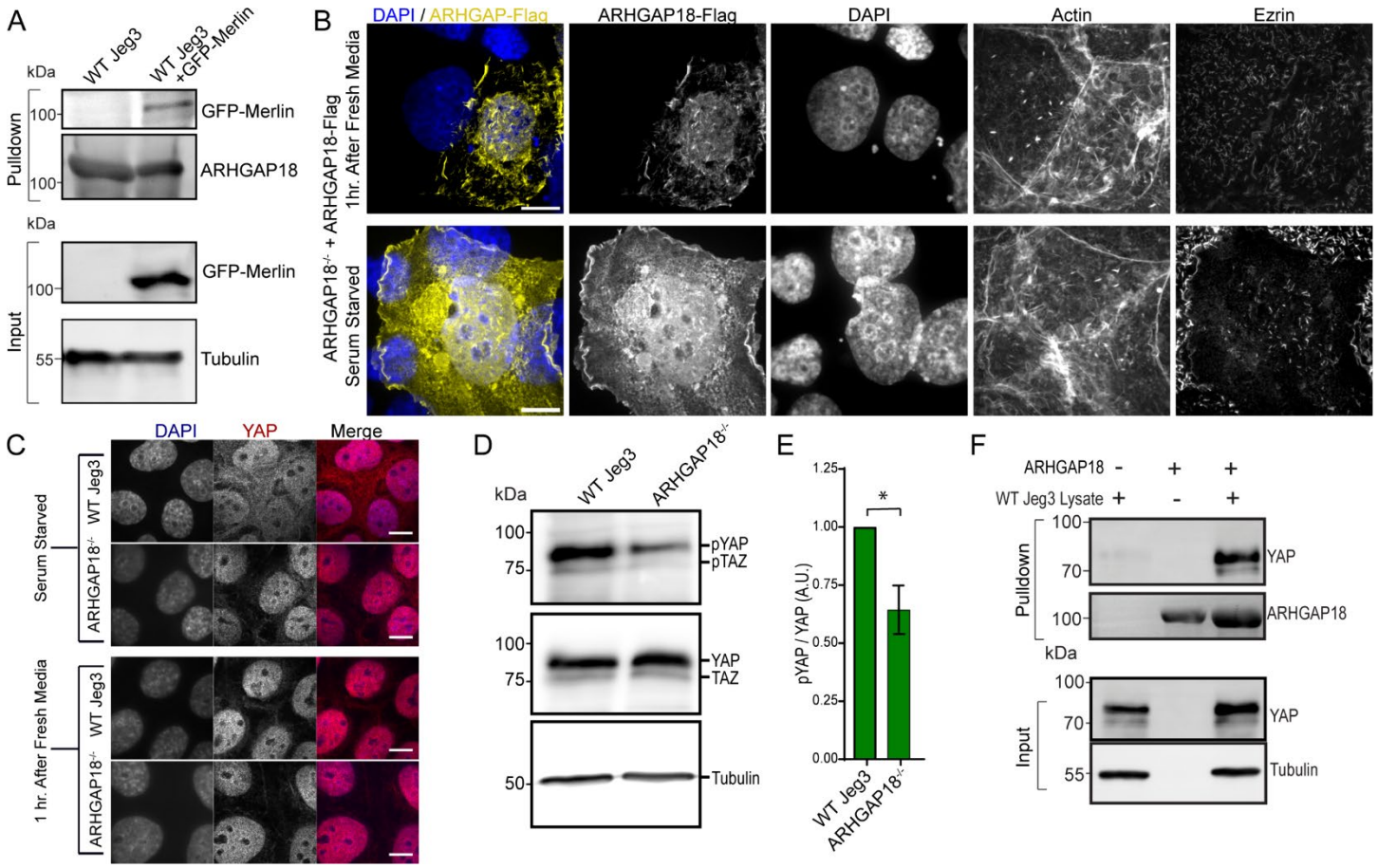

Figure 4: ARHGAP18 Complexes with YAP Affecting its Localization throughout the Cell Based on Nutrient Availability. A) Western blot of an ARHGAP18 pulldown from WT Jeg-3 cells with or without expression of GFP-merlin. B) Immunofluorescent imaging of ARHGAP18-flag rescue of ARHGAP18$^{-/-}$ cells in the serum starved or 1 hour after reintroduction of serum. ARHGAP18's localization includes the cytoplasm in the serum starved state. Ezrin staining of microvilli shows lower levels of microvilli in both conditions. Scale bar 10μm. C) Immunofluorescent imaging of YAP in WT and ARHGAP18$^{-/-}$ cells in the serum starved state or 1 hour after reintroduction of serum. YAP localization to the cytoplasm during serum starvation is lost in ARHGAP18$^{-/-}$ cells. Scale bar 10μm. D) Western blot of lysate from WT or ARHGAP18$^{-/-}$ cells shows a decrease in the phosphorylation of YAP and TAZ (pYAP/ pTAZ) in the knockout cells. E) Quantification of the band intensity of pYAP/YAP as shown by the blot in (D). Bars indicate Mean±SEM; conditions are significant by paired t-test ($p \leq 0.05$) n=3 F) Pulldown experiment using an ARHGAP18-agarose column. YAP does not bind to the column agarose alone nor is YAP present on the purified ARHGAP18 column before the addition of WT Jeg-3 lysate. When Jeg-3 lysate passed over the ARHGAP18 column endogenous YAP stably binds.

273 strongly to the nucleus and junctions while being almost entirely excluded from the
274 cytoplasm. Hippo pathway signaling responds to multiple external cues, including nutrient
275 availability to signal downstream transcription for cell proliferation and cytoskeletal
276 remodeling. When cells were deprived of serum, ARHGAP18's localization shifted to
277 include substantial cytoplasmic staining (Fig. 4B). Interestingly, ARHGAP18's localization
278 to microvilli and its reduction of the formation of microvilli was maintained in both
279 conditions, indicating that the microvilli specific functions were independent from nutrient
280 availability. We concluded that ARHGAP18 acted in part through a molecular interaction
281 with Merlin at junctions. However, the results also indicated that ARHGAP18 may have a
282 secondary, nuclear and cytoplasmic regulatory function depending on nutrient availability.

283 In serum-starved WT cells YAP is phosphorylated and localized to the cytoplasm.
284 Upon reintroduction of nutrients, YAP phosphorylation is reduced, and it is shuttled to the
285 nucleus, where it acts to promote cell proliferation and actin polymerization. Next, we
286 tested if YAP shuttling between the nucleus and cytoplasm in response to nutrient
287 availability was altered in Jeg-3 cells lacking ARHGAP18. We used immunofluorescent
288 staining of YAP and TAZ in cells fixed in either serum-fed or serum-starved states. In WT
289 serum-starved cells, YAP/TAZ showed diffuse staining throughout the cytoplasm and
290 nucleus (Fig. 4C). Upon reintroduction of serum into the media, YAP/TAZ's cytoplasmic
291 localization was lost within one hour, and only nuclear staining remained. In ARHGAP18
292 $^{-/-}$ cells YAP/TAZ remained predominantly in the nucleus in both the serum-starved and
293 serum-present media states. Using lysates from the serum-starved cells, we tested by
294 western blotting the phosphorylation state of YAP and TAZ (Fig. 4D). While the total
295 expression of YAP and TAZ remained the same in WT and ARHGAP18 KO cells, the

296 phosphorylation of YAP and TAZ was significantly reduced in the cells lacking ARHGAP18
297 compared to WT levels (Fig. 4D, E).

298 We hypothesized that ARHGAP18 may also form a complex with YAP that
299 influences YAP's cytoplasmic localization. To test this hypothesis, we passed WT Jeg-3
300 lysates over the immobilized ARHGAP18 column to probe for binding of native proteins
301 to ARHGAP18. We detected that endogenous YAP from WT Jeg-3 cells bound to
302 immobilized ARHGAP18 (Fig. 4F). We concluded that YAP's localization to the cytoplasm
303 in the serum starved state depended on the formation of a complex including both YAP
304 and ARHGAP18. The combined results indicate that ARHGAP18 acts as both a negative
305 RhoA regulator and as part of a Hippo signaling feedback loop between YAP and Merlin
306 to control polarized actin cytoskeletal structures.

307 **Discussion:**

308 Humans have 20 Rho/Ras family of GTPase genes where nucleotide state
309 transitions are accelerated by a plethora of guanine nucleotide exchange factors (GEFs)
310 and GTPase Activating Proteins (GAPs). This genetic complexity combined with partial
311 overlapping molecular functions, has presented significant challenges to the
312 characterization of the molecular functions of individual GAPs and GEFs in humans. For
313 example, of the approximately 83 GEFs in humans, at least 24 have specific or partial
314 activity for a single GTPase, RhoA (Vigil et al., 2010). Humans also have genes for three
315 dissociation inhibitors (RhoGDIs), which regulate Rho family localization through
316 membrane binding. Thus, much of our foundational understanding derives from careful
317 experimentation in more genetically advantageous model systems (Etienne-Manneville
318 and Hall, 2002). Here, we use CRISPR KO of human epithelial cells to investigate the

319 loss of a single RhoA effector, ARHGAP18. We uncover that ARHGAP18 forms
320 complexes with YAP and Merlin which drive interwoven molecular pathways regulating
321 actin organization, cell morphology, and junctional integrity. These results indicate that
322 Rho family effectors have the potential to act in complex and multifaceted cellular
323 functions linking multiple signaling and polarity-driving pathways.

324 We find the naming of the fly ortholog of ARHGAP18 as conundrum (Conu)
325 appropriate (Neisch et al., 2013). Our results add to multiple prior reports indicating that
326 ARHGAP18 has apparent contradictory additional cellular functions outside of Rho GAP
327 activity (Coleman et al., 2020; Lay et al., 2019; Neisch et al., 2013; Porazinski et al.,
328 2015). ARHGAP18 was first identified as a novel Rho effector in a microarray screen of
329 proteins regulating capillary tube formation by human umbilical vein endothelial cells
330 (Coleman et al., 2010). The fly ortholog conundrum (Conu) was subsequently reported to
331 localize to the cell cortex through a molecular interaction with the only fly ERM, Moesin
332 (Neisch et al., 2013). However, increased expression of conu did not produce a
333 phenotype typical of reduced levels of Rho1 as expected from a GAP and instead led to
334 proliferation and cell overgrowth. We identify the same unexpected phenotype in our
335 ARHGAP18 overexpression in human epithelial cells, where cells invade into neighboring
336 monolayers (Fig. 2C).

337 ARHGAP18$^{-/-}$ cells exhibit a near total loss of stress fibers (Fig. 1E, 2D) despite
338 increased cellular levels of pMLC (Fig. 1B) (Lombardo et al., 2024). These results
339 represent the strongest argument that ARHGAP18 functions in additionally alternative
340 pathways to RhoA/C alone. Our data raises several questions about how RhoA and YAP
341 are coordinated: First, what is the effect of ARHGAP18 complexing with both Merlin and

342 YAP? Loss of ARHGAP18 results in increased active RhoA at junctions (Lombardo et al.,
343 2024) promoting apical actin reorganization. Thus, it's reasonable to conclude that one of
344 Merlin's functions as a scaffolding protein is to sequester ARHGAP18 to junctions to
345 regulate RhoA locally (Fig. 5). When proliferative signaling is low, merlin is inactivated
346 and dissociates from the junctional cytoskeletal structures. Inactivation of Merlin would
347 mask the predicted binding site for ARHGAP18 in the conserved FERM domain shared
348 with ERMs. ARHGAP18 would then be free to complex with YAP in the cytosol. The
349 shuttling we characterize of ARHGAP18 localizing from junctions to the cytoplasm in
350 response to serum availability (Fig. 3A) matches this proposed mechanism (Fig.5). This
351 system would place ARHGAP18 as a signaling link between the Hippo and RhoA
352 cascades and as a component in a negative feedback loop between Merlin and YAP.

353 Second, why is non-muscle myosin 2 (NM-2) not producing actin bundles despite
354 being active in cells lacking ARHGAP18? The parameter space for defining this
355 phenotype makes experimentation extremely challenging as actin bundlers, nucleators,
356 severing proteins, and polymerization effectors may all be affected by the alterations to
357 YAP and RhoA in ARHGAP18$^{-/-}$ cells. The list of available mechanisms that YAP alone
358 may induce under perpetual nuclear localization (Fig. 4C) is daunting (Pocaterra et al.,
359 2020). However, our RNAseq analysis narrows the list of potential mechanisms (Fig. 3).
360 One potential explanation, supported by our RNA analysis, is the loss of the mechanical
361 attachment point for the stress fiber bundles at the basal membrane. Integrin expression
362 is severely disrupted in ARHGAP18 deficient cells (Fig. 3F-H) which would deprive a
363 forming actomyosin bundle from mechanically attaching to the plasma membrane.
364 Further insight into the potential mechanism driving the loss of stress fibers could come

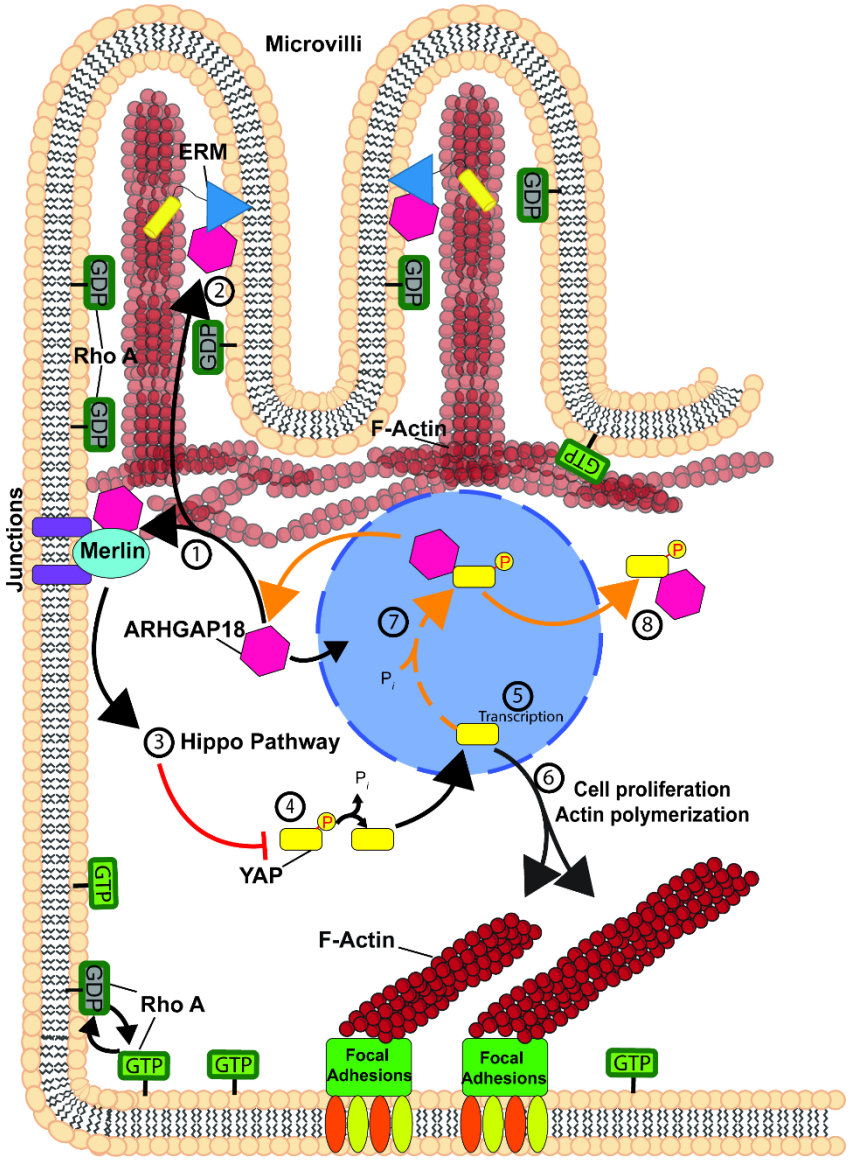

Figure 5: Model of ARHGAP18's coordination of RhoA and Hippo signaling pathways in Human epithelial cells. Under normal cellular conditions (black arrows), ARHGAP18 localizes to the nucleus, cell junctions, and microvilli. ARHGAP18 forms complexes with (1) Merlin at cell junctions and (2) ERMs in microvilli through direct binding to their conserved FERM domains. Once recruited to junctions by Merlin, ARHGAP18 regulates RhoA locally. Merlin simultaneously coordinates mechanosensation and proliferation signaling through activation of the hippo pathway. (4) Hippo signaling regulates the phosphorylation of YAP, where the active, dephosphorylated state is shuttled to the nucleus. (5) Active YAP/TAZ coordinate transcriptional changes which result in (6) expression of proteins regulating the actin cytoskeleton and proliferation. 7) Alternatively, when Hippo signaling suppresses YAP activation (orange arrows), YAP is phosphorylated through an ARHGAP18 dependent mechanism. 8) ARHGAP18 complexes with YAP which is required for proper phosphorylation and eventual shuttling of YAP to the cytosol for degradation. Loss of ARHGAP18 results in persistent localization of YAP to the nucleus with constitutively active proliferation signaling in addition to misregulation of RhoA at junctional and apical membranes. Without coordination of Hippo and RhoA signaling by ARHGAP18, knockout cells present a loss of stress fibers and filopodia at the basal surface through YAP signaling with disruption of microvilli actin core bundles and junctional integrity at the apical surface through RhoA signaling.

365 from predictive modeling using *silico* simulations. These have been productive in defining
366 the minimum components needed to organize complex cytoskeletal behaviors (Landino
367 et al., 2021; Walcott and Warshaw, 2022). This approach will likely be needed in future
368 investigations to predict how alterations in actin filament and myosin dynamics prevent
369 stress fiber formation in ARHGAP18$^{-/-}$ cells. Prior experimental work can also provide
370 some clues to NM-2 overactivation resulting in a loss of actin bundles. In microvilli the
371 loss of ARHGAP18 results in overactivation of NM-2 (specifically isoform MHY14) where
372 motors produce enough force to shred the actin bundles of microvilli (Lombardo et al.,
373 2024). This mechanism occurs to a lesser extent in the apical terminal web of actin in WT
374 epithelial cells through NM-2C (Chinowsky et al., 2020). The force required to dissociate
375 individual actin filaments from a bundle crosslinked by fimbrin (microvilli), fascin
376 (filopodia), or alpha actinin (stress fibers) is unknown and will require careful *in vitro*
377 biophysical assays using atomic force microscopy or optical tweezers to define.

378 Regardless of the genetic background, a major technical challenge for the study
379 of Rho-dependent signaling pathway's regulation of cellular actin architecture is that 1)
380 actin is the most abundant protein in the cytosol, 2) actin forms three-dimensional
381 interwoven webs of densely packed networks, 3) filaments can turn over on the scale of
382 30-60 seconds, and 4) the single filament structure is 7 nanometers across (two orders
383 of magnitude below the diffraction limit of visible light). We've overcome these hurdles
384 using super-resolution STORM microscopy (Xu et al., 2012). While multiple prior studies
385 have observed the change in actin bundles of cells with altered ARHGAP18 levels
386 (Coleman et al., 2020; Neisch et al., 2013; Porazinski et al., 2015), our super resolution
387 characterization allows for the dissection of the exact actin structures lost. Reorganization

388 toward branched or individual filaments would dramatically alter the transport of
389 intracellular cargos by myosin and microtubule-based motors (Bensel et al., 2024; Heaslip
390 et al., 2014; Lombardo et al., 2017; Lombardo et al., 2019). Our STORM data indicates
391 that not all actin or bundles are lost as it appears by our own traditional confocal staining
392 (Compare Fig. 2A to Fig.1E). Instead, significant quantities of single filaments are
393 maintained in areas that appear devoid of actin under conventional light microscopy.
394 When these findings are combined with our RNAseq data the molecular pathways
395 responsible for these changes were identified to be a combination of RhoA signaling and
396 pathways both upstream and downstream of YAP/TAZ. Our data indicates that the loss
397 of ARHGAP18 switches the epithelial cell's basal actin signaling toward a state where the
398 actin architecture resembles a leading edge comprised of single and branching filaments.
399 Consequently, Jeg-3 cells which typically form monolayers, instead form 3-dimensional
400 stacks on top of their neighboring cells when ARHGAP18 signaling is disrupted (Fig. 2C)

401 Collectively, our results support a model where loss of ARHGAP18 depolarizes
402 cells by dysregulating apical, junctional, and basal membrane identification through
403 ERMs, Merlin, and YAP, respectively. The exact molecular interactors responsible for the
404 signaling cascade that results in pMLC activation in the overexpression of ARHGAP18
405 will require future characterization. Additional investigation of the molecular details of the
406 ARHGAP18/YAP binding complex will elucidate the mechanism that ARHGAP18 uses to
407 coordinate RhoA signaling with the Hippo pathway to define cell polarity and morphology.

408

409 **Methods:**

410 Reagents and cDNAs

411 Anti-ezrin antibody (CPTC-ezrin-1 supernatant concentrate obtained from the
412 Developmental Studies Hybridoma Bank; catalog no. CPTC-Ezrin-1; Research Resource
413 Identification AB_2100318) was used 1:100 for immunofluorescence. Mouse anti-Flag
414 (Sigma-Aldrich; catalog no. F1804) was used at 1:250 for immunofluorescence and
415 1:5,000 for Western blot, and mouse anti-tubulin (Sigma-Aldrich; catalog no. T5168) was
416 used at 1:5,000 for Western blot. anti-MLC2 (catalog no. 3672) and anti–phospho-MLC2
417 (phospho-Thr18/Ser19; catalog no. 3674) were purchased from Cell Signaling
418 Technology and used at 1:500 in Western blots. Anti–nonmuscle myo-IIB from BioLegend
419 (catalog no. 909902) and non-muscle myo-IIA (BioLegend; catalog no. 909802) were
420 used at 1:100 in both Western blots and immunofluorescence. The rabbit ARHGAP18
421 antibody was produced and characterized previously (Lombardo et al., 2024) and used
422 at 1:500 for western blotting. The rabbit anti-vinculin antibody was a kind gift of A.
423 Bretscher and was described previously (Franck et al., 1990) and used at 1:200 for
424 immunofluorescence. For actin staining, Alexa Fluor 647 phalloidin (Invitrogen; catalog
425 no. A30107) was used at 1:250.

426 Human ARHGAP18 constructs were produced using polymerase chain reaction (PCR)
427 with New England Biolabs (NEB) Phusion High-Fidelity PCR Kit (Cat# E0553L). cDNA of
428 ARHGAP18 was obtained off a construct originally derived from the Harvard Plasma
429 Database (ID # HsCD00379004). NEB Monarch PCR & DNA Cleanup Kits (Cat# T1030S)
430 and Thermo Scientific GeneJET Gel Extraction Kits (Cat# K0692) were used to purify
431 PCR and Gibson Assembly products. DNA products were cloned into the mammalian
432 expression vector PQCXIP using NEB Gibson Assembly cloning Kit (Cat# E5510S).

433 transformations were done into OneShot TOP10 bacteria (Thermo Fisher; Cat#
434 C404010), selected using ampicillin resistance, and then sequenced for verification. GFP-
435 merlin was a gift of A. Bretscher and produced previously (Sher Bretscher Dev Cell 2012)

436 Western Blotting:

437 Western blot analysis of cell lysates was done using 4–12% Thermo Fisher bolt SDS-
438 PAGE gels (Cat# NW04120). Gels were transferred to a polyvinylidene difluoride (PVDF)
439 membrane using a BioRad Transblot Turbo (Cat# 1704150) and blocked with 5% milk in
440 Tris Buffered Saline (TBS) + 0.5% Tween-20 (TBST). For detecting MLC and pMLC, 0.2-
441 µm pore size PVDF (EMD Millipore; Immobilon-PSQ) was used. Primary antibodies were
442 incubated with the membrane in TBST supplemented with 5% BSA either for 1 hr at room
443 temperature or overnight at 4°C. Bands were detected with infrared fluorescent secondary
444 antibodies (Invitrogen or LI-COR Biosciences; catalog nos. 926-32221 and 926-32210).
445 Membranes were imaged using a Bio-Rad MP ChemiDoc. ImageJ intensity profile built-
446 in toolset was used for western blotting quantification, which was then averaged,
447 normalized, and plotted in Microsoft Excel.

448 Immunofluorescent Imaging:

449 Room temperature (23°C) fixed cell confocal imaging was done using a spinning-disk
450 (Yokogawa CSU-X1; Intelligent Imaging Innovations) Leica DMi600B microscope with a
451 spherical aberration correction device and either a ×100/1.46 NA Leica objective.
452 Hamamatsu ORCA-Flash 4.0 camera metal-oxide semiconductor device was used to
453 capture images, and Z-slices of acquired images were assembled using SlideBook 6
454 software (Intelligent Imaging Innovations). Maximum-intensity projections were

455 assembled in SlideBook 6 or ImageJ and exported to Adobe Illustrator for editing. Vertical
456 expansion of side projections was used to increase visual clarity of apical/basal
457 localization. Widefield microscopy was performed using an inverted Leica DMi8 widefield
458 microscope equipped with a Leica ×100 NA air objective, a Leica DFC 9000 GTC camera,
459 Leica Application Suite X, and Leica adaptive focus control.

460 Immobilized ARHGAP18 pulldowns:

461 To determine the interaction between ARHGAP18 and Merlin or YAP, pulldown assays
462 were performed using cell lysate from Jeg-3 WT cells. Purified human ARHGAP18 was
463 produced by bacterial expression of an N-terminal-SUMO-HIS-tagged protein purified
464 using a NiNTA resin as described in (Lombardo et al., 2024). Transfections for GFP Merlin
465 were performed using PEI MAX polyethylenimine reagent (Polysciences; Cat# 24765).
466 Cells were harvested with lysis buffer (25 mM Tris, 5% glycerol, 150 mM NaCl, 50 mM
467 NaF, 0.1 mM Na3VO4, 10mM βGP, 0.2% Triton X-100, 250 mM calyculin A, 1 mM DTT,
468 1× cOmplete Protease Inhibitor Cocktail [Roche; Cat# 11836153001]) by scraping.
469 Lysates were then sonicated, and centrifuged at 8000 × g for 10 min at 4°C. Before
470 incubating with the cell lysates, SUMO-ARHGAP18 NiNTA beads were equilibrated and
471 washed into lysis buffer. The sample of the supernatant was taken for input, then the rest
472 was added to the SUMO-ARHGAP18 NiNTA beads and nutated for 3 hr at 4°C. After
473 incubation, the beads were pelleted and washed four times with a 2 minute incubation
474 before boiling in 40 µL 2× Laemmli sample buffer.

475 RNA-Seq Sample Preparation

476 Cells were plated in 100mm Corning 100 × 20 mm Petri-style TC-treated culture dishes
477 (Cat# 430167) and allowed to grow to 80% confluency. Cells were plated at 10am on day
478 0, media was exchanged at 10am on day 1 and cells were collected and pelleted at 10am
479 on day 2 over a total of 48 hours to maintain environmental consistency. Pelleting of cells
480 was performed by washing the cells 3 times in PBS then adding 0.05% trypsin (Thermo
481 Fisher Scientific; Cat# 25300054) and incubating at 37°C and 5% CO2 for 5 minutes.
482 Once detached cells were washed into MEM media (Thermo Fisher Scientific; Cat#
483 10370088) then the media was exchanged for ice cold PBS. Cells were pelleted at 1000x
484 g and stored at -80C until they were lysed for RNA extraction. Total RNA was extracted
485 at the University at Buffalo Core Genomics Facility using TRIzol reagent (cat. no.
486 15596018, Invitrogen). It was then purified with an RNeasy kit (cat. no. 74106, Qiagen).
487 Libraries were prepared using the Illumina TruSeq Stranded total RNA kit and the Ribo-
488 Zero plus rRNA depletion kit. The sequencing was performed on an Illumina HiSeq 4000
489 PE100 sequencer. The nf-core/rnaseq Version 3.18.0 bioinformatics pipeline was used to
490 analyze RNA sequencing data with alignment and quantification performed using STAR
491 (Dobin et al., 2013) followed by Salmon (Patro et al., 2017).

492 Bioinformatic analysis

493 Raw gene counts were analyzed using DESeq2 package in R to identify differentially
494 expressed genes (DEGs) between WT-Jeg3 and ARHGAP18 KO conditions. Genes were
495 classified as DEGs if the following filtering criteria were met: false-discovery rate (FDR)
496 adjusted p-value of < 0.05 and absolute $\log_2$(fold-change) of > 0.5. Sample distribution
497 was visualized with the Principal Component Analysis (PCA) plot generate by ggplot2

498 package in R using a normalized count dataset. Python's bioinfokit was used to create
499 the volcano plot.

500 Functional enrichment analysis was performed using the g:GOSt function on the gProfiler
501 web server (https:// biit.cs.ut.ee/gprofiler/gost) with the identified DEGs. The significance
502 threshold was set to FDR value, and significant Gene Ontology (GO) terms in molecular
503 functions, biological pathways, and cellular components categories were defined by an
504 adjusted p-value of < 0.05. The top 15 GO terms in each category were visualized using
505 bubble plots generated by SRplot online server.

506 To visualize expression patterns across samples, clustered heatmap was generated with
507 SRplot online server using $\log_2$-transformed normalized gene, expression values.
508 Specifically, hierarchical clustering was performed on both genes (rows) and samples
509 (columns) using Euclidean distance and complete linkage cluster methods. Genes
510 visualized were DEGs annotated in the GO term.

511 Ingenuity pathway analysis (IPA, QIAGEN) was used to perform network analysis on 889
512 DEGs identified in this dataset. A core analysis was run on this dataset, which produced
513 information on various mechanistic pathways and enriched function-based literature
514 gathered in IPA knowledge base. Specifically, we used the "My Pathway" function to
515 generate predicted networks between ARHGAP18 and some genes of interest. The
516 "Molecular Activity Predictor" tool was used to elucidate predicted activation states of
517 molecules and interactions downstream of ARHGAP18.

518

519 <u>Cell culture and expression vectors:</u>

520 Jeg3 cells were purchased from ATCC.org (Cat# Htb-36) and maintained in a humidified
521 incubator at 37°C and 5% CO2. Media for Jeg3 cells used in 1× MEM (Thermo Fisher
522 Scientific; Cat# 10370088) with penicillin/streptomycin (Thermo Fisher Scientific; Cat#
523 15070063), 10% fetal bovine serum (FBS; Thermo Fisher Scientific; Cat# 26140079), and
524 GlutaMAX (Thermo Fisher Scientific; Cat# 35050061). Corning 100 × 20 mm Petri-style
525 TC-treated culture dishes (Cat# 430167) were used for maintaining cultures. Transient
526 transfections used a PEI MAX polyethylenimine reagent (Polysciences; Cat# 24765). All
527 cell lines were checked for mycoplasma in regular intervals using DAPI staining.
528 ARHGAP18 knockout cells were created and characterized (Lombardo et al., 2024). In
529 summary of these methods, multiple CRISPR single-guide RNAs against the sequence
530 5′-CAGCGGCAAGGACCAGACCG-3′ or 5′-CAGCGGCAAGGACCAGACCG-3′ were
531 cloned into puromycin-resistant pLenti-CRISPRV2 (Addgene; Cat# 49535) which was
532 transfected into 293TN cells with psPAX3 and pCMV-VSV-G (a gift from Jan Lammerding,
533 Weill Institute for Cell and Molecular Biology, Cornell University, Ithaca, NY) for 48–72 hr.
534 Jeg3 cells were then transduced with virus supplemented with Polybrene to 8 µg/mL twice
535 a day for 2 days, followed by puromycin selection at 2 µg/mL. Mixed populations of
536 selected cells were single-cell sorted and then screened by western blotting. ARHGAP18
537 expression vectors were created and described in (Lombardo et al., 2024).

538 <u>Super-Resolution STORM:</u>

539 Jeg-3 cells were plated on 35 mm 1.5 high precision glass bottom MatTek dishes (Cat#
540 P35G-0.170-14-C) and fixed and permeabilized using 2mLs of 0.3% glutaraldehyde and
541 0.25% Triton X-100 in cytoskeleton buffer (10 mM MES pH 6.1, 150 mM NaCl, 5 mM
542 EGTA, 5 mM glucose, and 5 mM $MgCl_2$) for 1-2 min at room temperature. Initial fixation

543 was followed by 2% glutaraldehyde in cytoskeletal buffer for 10 min at room temperature.
544 The sample was then treated with 1mL 0.1% NaBH4 in Phosphate Buffered Saline (PBS)
545 at pH 7.4 for 7 min to reduce background fluorescence. Actin was stained in phalloidin at
546 a dilution of 1:250 overnight at 4°C. Slides were washed into 50mM Tris, pH 8.0, 10%
547 glucose, 10mM NaCl, 0.5mg/ml Glucose oxidase, 0.04 mg/ml catalase with 10%
548 cysteamine by weight, and 1.5% 2-Mercaptoethanol (BME) by weight. Stochastic Optical
549 Reconstruction Microscopy (STORM)(Rust et al., 2006) was performed using a Zeiss
550 Elyra super-resolution inverted Axio Observer.Z1 microscope provided by Cornell
551 University's Institute of Biotechnology Imaging Facility. Lasers emitting 405 and 640 nm
552 wavelengths through a 100x/1.46 NA oil objective captured images on a pco.edge 5.5m
553 camera. Exposure time ranged from 50 to 400 ms and was dependent on the sample and
554 channel to optimize STORM reconstruction. A minimum of 100,000 images were used for
555 each STORM processing using the Imagej ThunderSTORM toolset (Ovesny et al., 2014)
556 or The Zeiss Zen built-in STORM reconstruction toolset and adjusting the filtering
557 conditions to maximize the signal to noise of single actin filaments in reconstructions.

558 Statistical Methods:

559 Statistical comparisons were performed in Microsoft Excel. The type of statistical tests
560 utilized, the configuration of error bars, and the number of independent data points (*n*)
561 are detailed in the figure legends respective to the data tested. Nonparametric or
562 parametric testing was justified through the assumption of the tested data to have a
563 normal distribution or not. Analyses were also done using GraphPad Prism to produce a
564 graphical representation of the amount of phosphorylated YAP over the total expression
565 of YAP with the test and *n* listed in the figure legend.

Acknowledgements:

We thank A. Bretscher and R. Visawantha for their kind gift of the human ARHGAP18 plasmid. We thank A. Martin for their critical comments on the data interpretation. Funding was supported by the National Institutes of Health grant R35GM156870 to A.T.L. and grant R01HL163168 to Y.B.. Preliminary data was collected under NIH grant R35GM131751 to A. Bretscher. We thank A. Heaslip and N. Bouffard for their expertise in troubleshooting STORM. Super resolution microscopy was performed at both the Microscopy Imaging Center at the University of Vermont (RRID# SCR_018821), and the Cornell Institute of Biotechnology Imaging Facility supported by the National Science Foundation funding (1428922).

Citations:

Bensel, B.M., S.B. Previs, C. Bookwalter, K.M. Trybus, S. Walcott, and D.M. Warshaw. 2024. Kinesin-1-transported liposomes prefer to go straight in 3D microtubule intersections by a mechanism shared by other molecular motors. *Proc Natl Acad Sci U S A*. 121:e2407330121.

Chang, G.H., A.J. Lay, K.K. Ting, Y. Zhao, P.R. Coleman, E.E. Powter, A. Formaz-Preston, C.J. Jolly, N.I. Bower, B.M. Hogan, S. Rinkwitz, T.S. Becker, M.A. Vadas, and J.R. Gamble. 2014. ARHGAP18: an endogenous inhibitor of angiogenesis, limiting tip formation and stabilizing junctions. *Small GTPases*. 5:1-15.

587 Chinowsky, C.R., J.A. Pinette, L.M. Meenderink, K.S. Lau, and M.J. Tyska. 2020. Nonmuscle
588 myosin-2 contractility-dependent actin turnover limits the length of epithelial
589 microvilli. *Mol Biol Cell*. 31:2803-2815.
590 Coleman, P.R., C.N. Hahn, M. Grimshaw, Y. Lu, X. Li, P.J. Brautigan, K. Beck, R. Stocker, M.A.
591 Vadas, and J.R. Gamble. 2010. Stress-induced premature senescence mediated by a
592 novel gene, SENEX, results in an anti-inflammatory phenotype in endothelial cells.
593 *Blood*. 116:4016-4024.
594 Coleman, P.R., A.J. Lay, K.K. Ting, Y. Zhao, J. Li, S. Jarrah, M.A. Vadas, and J.R. Gamble. 2020.
595 YAP and the RhoC regulator ARHGAP18, are required to mediate flow-dependent
596 endothelial cell alignment. *Cell Commun Signal*. 18:18.
597 Denk-Lobnig, M., and A.C. Martin. 2019. Modular regulation of Rho family GTPases in
598 development. *Small GTPases*. 10:122-129.
599 Dobin, A., C.A. Davis, F. Schlesinger, J. Drenkow, C. Zaleski, S. Jha, P. Batut, M. Chaisson, and
600 T.R. Gingeras. 2013. STAR: ultrafast universal RNA-seq aligner. *Bioinformatics*. 29:15-
601 21.
602 Etienne-Manneville, S., and A. Hall. 2002. Rho GTPases in cell biology. *Nature*. 420:629-635.
603 Franck, Z., M. Footer, and A. Bretscher. 1990. Microinjection of villin into cultured cells
604 induces rapid and long-lasting changes in cell morphology but does not inhibit
605 cytokinesis, cell motility, or membrane ruffling. *J Cell Biol*. 111:2475-2485.
606 Gaeta, I.M., L.M. Meenderink, M.M. Postema, C.S. Cencer, and M.J. Tyska. 2021. Direct
607 visualization of epithelial microvilli biogenesis. *Curr Biol*. 31:2561-2575 e2566.
608 Hall, A. 1998. Rho GTPases and the actin cytoskeleton. *Science*. 279:509-514.

609 Hall, A., and C.D. Nobes. 2000. Rho GTPases: molecular switches that control the
610 organization and dynamics of the actin cytoskeleton. *Philos Trans R Soc Lond B Biol*
611 *Sci*. 355:965-970.
612 Harvey, K.F., X. Zhang, and D.M. Thomas. 2013. The Hippo pathway and human cancer. *Nat*
613 *Rev Cancer*. 13:246-257.
614 Heaslip, A.T., S.R. Nelson, A.T. Lombardo, S. Beck Previs, J. Armstrong, and D.M. Warshaw.
615 2014. Cytoskeletal dependence of insulin granule movement dynamics in INS-1 beta-
616 cells in response to glucose. *PLoS One*. 9:e109082.
617 Jackson, J.A., M. Denk-Lobnig, K.A. Kitzinger, and A.C. Martin. 2024. Change in RhoGAP and
618 RhoGEF availability drives transitions in cortical patterning and excitability in
619 Drosophila. *Curr Biol*. 34:2132-2146 e2135.
620 Julian, L., and M.F. Olson. 2014. Rho-associated coiled-coil containing kinases (ROCK).
621 *Small GTPases*.
622 Landino, J., M. Leda, A. Michaud, Z.T. Swider, M. Prom, C.M. Field, W.M. Bement, A.G.
623 Vecchiarelli, A.B. Goryachev, and A.L. Miller. 2021. Rho and F-actin self-organize
624 within an artificial cell cortex. *Curr Biol*. 31:5613-5621 e5615.
625 Lay, A.J., P.R. Coleman, A. Formaz-Preston, K.K. Ting, B. Roediger, W. Weninger, M.A.
626 Schwartz, M.A. Vadas, and J.R. Gamble. 2019. ARHGAP18: A Flow-Responsive Gene
627 That Regulates Endothelial Cell Alignment and Protects Against Atherosclerosis. *J Am*
628 *Heart Assoc*. 8:e010057.

629 Lombardo, A.T., C.A. Mitchell, R. Zaman, D.J. Mcdermitt, and A. Bretscher. 2024. ARHGAP18-
630 ezrin functions as an autoregulatory module for RhoA in the assembly of distinct
631 actin-based structures. *Elife*. 13.
632 Lombardo, A.T., S.R. Nelson, M.Y. Ali, G.G. Kennedy, K.M. Trybus, S. Walcott, and D.M.
633 Warshaw. 2017. Myosin Va molecular motors manoeuvre liposome cargo through
634 suspended actin filament intersections in vitro. *Nat Commun*. 8:15692.
635 Lombardo, A.T., S.R. Nelson, G.G. Kennedy, K.M. Trybus, S. Walcott, and D.M. Warshaw.
636 2019. Myosin Va transport of liposomes in three-dimensional actin networks is
637 modulated by actin filament density, position, and polarity. *Proc Natl Acad Sci U S A*.
638 116:8326-8335.
639 Maeda, M., H. Hasegawa, T. Hyodo, S. Ito, E. Asano, H. Yuang, K. Funasaka, K. Shimokata, Y.
640 Hasegawa, M. Hamaguchi, and T. Senga. 2011. ARHGAP18, a GTPase-activating
641 protein for RhoA, controls cell shape, spreading, and motility. *Mol Biol Cell*. 22:3840-
642 3852.
643 Miller, M.R., D.J. McDermitt, C. Sauvanet, A.T. Lombardo, R. Zaman, and A. Bretscher. 2022.
644 The RabGAPs EPI64A and EPI64B regulate the apical structure of epithelial cells. *Mol*
645 *Biol Cell*. 33.
646 Morales, E.A., I. Gaeta, and M.J. Tyska. 2023. Building the brush border, one microvillus at a
647 time. *Curr Opin Cell Biol*. 80:102153.
648 Neisch, A.L., E. Formstecher, and R.G. Fehon. 2013. Conundrum, an ARHGAP18 orthologue,
649 regulates RhoA and proliferation through interactions with Moesin. *Mol Biol Cell*.
650 24:1420-1433.

651 Ovesny, M., P. Krizek, J. Borkovec, Z. Svindrych, and G.M. Hagen. 2014. ThunderSTORM: a
652 comprehensive ImageJ plug-in for PALM and STORM data analysis and super-
653 resolution imaging. *Bioinformatics*. 30:2389-2390.
654 Patro, R., G. Duggal, M.I. Love, R.A. Irizarry, and C. Kingsford. 2017. Salmon provides fast and
655 bias-aware quantification of transcript expression. *Nat Methods*. 14:417-419.
656 Pocaterra, A., P. Romani, and S. Dupont. 2020. YAP/TAZ functions and their regulation at a
657 glance. *J Cell Sci*. 133.
658 Porazinski, S., H. Wang, Y. Asaoka, M. Behrndt, T. Miyamoto, H. Morita, S. Hata, T. Sasaki,
659 S.F.G. Krens, Y. Osada, S. Asaka, A. Momoi, S. Linton, J.B. Miesfeld, B.A. Link, T. Senga,
660 N. Shimizu, H. Nagase, S. Matsuura, S. Bagby, H. Kondoh, H. Nishina, C.P.
661 Heisenberg, and M. Furutani-Seiki. 2015. YAP is essential for tissue tension to ensure
662 vertebrate 3D body shape. *Nature*. 521:217-221.
663 Priya, R., K. Wee, S. Budnar, G.A. Gomez, A.S. Yap, and M. Michael. 2016. Coronin 1B
664 supports RhoA signaling at cell-cell junctions through Myosin II. *Cell Cycle*. 15:3033-
665 3041.
666 Reginensi, A., L. Enderle, A. Gregorieff, R.L. Johnson, J.L. Wrana, and H. McNeill. 2016. A
667 critical role for NF2 and the Hippo pathway in branching morphogenesis. *Nat*
668 *Commun*. 7:12309.
669 Rust, M.J., M. Bates, and X. Zhuang. 2006. Sub-diffraction-limit imaging by stochastic optical
670 reconstruction microscopy (STORM). *Nat Methods*. 3:793-795.

671 Sepaniac, L.A., N.R. Davenport, and W.M. Bement. 2023. Bring the pain: wounding reveals a
672 transition from cortical excitability to epithelial excitability in Xenopus embryos. *Front*
673 *Cell Dev Biol*. 11:1295569.
674 Swider, Z.T., A. Michaud, M. Leda, J. Landino, A.B. Goryachev, and W.M. Bement. 2022. Cell
675 cycle and developmental control of cortical excitability in Xenopus laevis. *Mol Biol*
676 *Cell*. 33:ar73.
677 Vigil, D., J. Cherfils, K.L. Rossman, and C.J. Der. 2010. Ras superfamily GEFs and GAPs:
678 validated and tractable targets for cancer therapy? *Nat Rev Cancer*. 10:842-857.
679 Walcott, S., and D.M. Warshaw. 2022. Modeling myosin Va liposome transport through actin
680 filament networks reveals a percolation threshold that modulates transport
681 properties. *Mol Biol Cell*. 33:ar18.
682 Xu, K., H.P. Babcock, and X. Zhuang. 2012. Dual-objective STORM reveals three-dimensional
683 filament organization in the actin cytoskeleton. *Nat Methods*. 9:185-188.
684 Zaman, R., A. Lombardo, C. Sauvanet, R. Viswanatha, V. Awad, L.E.R. Bonomo, D.
685 McDermitt, and A. Bretscher. 2021. Effector-mediated ERM activation locally inhibits
686 RhoA activity to shape the apical cell domain. *J Cell Biol*. 220.
687 Zanconato, F., M. Cordenonsi, and S. Piccolo. 2016. YAP/TAZ at the Roots of Cancer. *Cancer*
688 *Cell*. 29:783-803.

689